International Journal of Modern Physics D

Ellipticity of Structures in CMB Sky Maps

Ralf Aurich, Holger S. Janzer, Sven Lustig

Institut für Theoretische Physik, Universität Ulm,
Albert-Einstein-Allee 11, D-89069 Ulm, Germany

Frank Steiner

Université Lyon 1, Centre de Recherche Astrophysique de Lyon
CNRS UMR 5574, 9 avenue Charles André, F-69230 Saint-Genis-Laval, France

We study the ellipticity of contour lines in the sky maps of the cosmic microwave background (CMB) as well as other measures of elongation. The sensitivity of the elongation on the resolution of the CMB maps which depends on the pixelization and the beam profile of the detector, is investigated. It is shown that the current experimental accuracy does not allow to discriminate between cosmological models which differ in curvature by $\Delta\Omega_{\rm tot} = 0.05$. Analytical expressions are given for the case that the statistical properties of the CMB are those of two-dimensional Gaussian random fields.

Keywords: cosmology, cosmic microwave background, statistic, Gaussian random fields

1. Introduction

The cosmic microwave background (CMB) gives a wealth of information about the Universe. The usual statistical analysis comprises the angular auto-correlation function $C(\vartheta)$ as well as the angular power spectrum δT_l^2, which lead to an improved determination of the cosmological parameters. Besides these statistics there are topological/geometrical descriptors of the CMB such as the number densities of maxima and minima, the ellipticities of the peaks, and peak correlation properties. Under the assumption that the CMB has the statistical properties of two-dimensional homogeneous and isotropic Gaussian random fields, the theoretical predictions are derived in Ref. 1.

This paper deals with the structure of the contour lines of a given temperature level δT in the CMB maps. In the vicinity of extrema these contour lines can be approximated by ellipses having the ellipticity E

$$E := \frac{a}{b} \quad , \quad E \geq 1 \quad , \tag{1}$$

where $a \geq b$ denote the major and minor semi-axes of the ellipses which best match the contour line around a given peak. The interesting question is how the ellipticities are distributed for a given map in dependence on the temperature level δT. This provides a further test[2,3] of Gaussianity by comparing the ellipticities with the corresponding results of two-dimensional Gaussian random fields[1]. In Refs. 4, 5, 6 it is

shown, however, that there are better geometrical estimators as tests of Gaussianity than the ellipticity like the Gaussian curvature. Therefore, the main motivation for this paper is to study the discrepancy of the ellipticity between the observations and simulations of the CMB as reported in Refs. 7, 8, 9, 10, 11, 12. In these papers an excess in the ellipticity $E = 2.2 \ldots 2.7$ is found compared to standard ΛCDM models having E around 1.65. Due to noise and the foreground uncertainties it is difficult to obtain the ellipticity from the measured CMB radiation. The ellipticity was determined from the COBE-DMR map[7] and from the BOOMERanG map[8,9]. These results are confirmed by the analysis of the WMAP 1yr data[10,11] and the 3yr data[12]. Furthermore, a strong dependence of the ellipticity on the curvature of the Universe is claimed and, with respect to the excess ellipticity, this is interpreted as a hint towards a hyperbolic Universe. In Ref. 4 there is no such ellipticity-curvature correlation found by studying low Ω and flat universes based on CDM models. Thus there remains the question whether the excess ellipticity is real and how such an excess, if present, has to be interpreted.

2. CMB Sky Maps

2.1. *Cosmological models*

The standard ΛCDM model of cosmology is given by a certain set of cosmological parameters. The curvature of the universe is determined by the value of the total energy density $\Omega_{\rm tot}$ at the present epoch which is the sum

$$\Omega_{\rm tot} \;=\; \Omega_\Lambda + \Omega_{\rm cdm} + \Omega_{\rm b} + \Omega_{\rm r} \tag{2}$$

of the energy density Ω_Λ of dark energy, $\Omega_{\rm cdm}$ of cold dark matter, $\Omega_{\rm b}$ of baryonic matter and $\Omega_{\rm r}$ of radiation. A value $\Omega_{\rm tot} > 1$, $= 1$ or < 1 reveals a spherical, flat or hyperbolic universe, respectively. The concordance ΛCDM model[13,14] leads to a flat universe where the angular power spectrum $\delta T_l^2 = l(l+1)C_l/(2\pi)$ has the first acoustic peak at $l \simeq 220$. The following analysis investigates the dependence of the ellipticity on the curvature of the universe. To that aim only the amount of dark energy Ω_Λ is varied, all other cosmological parameters are those of the ΛCDM concordance model.

In addition to the infinite volume ΛCDM concordance model, a model with a cubic topology[15,16] is also studied which has a finite volume and is statistically anisotropic. This model thus violates some conditions required for the following analytical expressions as outlined in the Appendix. This model serves as a test whether an anisotropic non-trivial topology can be discerned by an elongation measure. The sky maps are simulated for the cubic topology using the same cosmological parameters as for the infinite concordance model. The side length L of this toroidal topology is chosen as $L = 3.86\, L_H$ where L_H is the Hubble length. For this length L a better agreement with the correlations observed in the CMB sky is found[15,16,17] than for the ΛCDM concordance model. The eigenmodes belonging to the first 50 000 eigenvalues for the cubic topology are used for the simulation, i. e. a total of 61 556 892

eigenmodes. Furthermore, the eigenmodes are expanded in the spherical basis up to $l_{\max} = 1000$ yielding sky maps with structures beyond the third acoustic peak where the Silk damping already smoothes a further fine-structure. In this way CMB sky simulations are obtained for which resolution effects can be studied.

For a given cosmological model, i. e. a given set of cosmological parameters, one can calculate the multipole spectrum

$$C_l \;:=\; \left\langle \frac{1}{2l+1} \sum_{m=-l}^{l} |a_{lm}|^2 \right\rangle \quad , \tag{3}$$

where a_{lm} are complex coefficients obtained from the expansion of a CMB sky map $\delta T(\theta, \phi)$ into spherical harmonics $Y_{lm}(\phi, \theta)$ due to

$$\delta T(\theta, \phi) \;=\; \sum_{l=0}^{\infty} \sum_{m=-l}^{l} a_{lm} Y_{lm}(\phi, \theta) \quad . \tag{4}$$

The multipole spectrum C_l is obtained from an ensemble average denoted by $\langle \ldots \rangle$ over infinitely many realisations of universes with fixed cosmological parameters. The deviation of the multipole spectrum C_l of an individual realisation from the ensemble average is characterised by the cosmic variance

$$\mathrm{Var}(C_l) \;:=\; \frac{2C_l^2}{2l+1} \quad , \tag{5}$$

where one has to assume that the CMB is a homogeneous isotropic Gaussian random field. This has to be taken into account by comparing theory and experiment.

2.2. *Resolution of the sky maps*

Statistical measures of the niveau lines depend sensitively on the resolution of the sky maps. Thus a few remarks are in order. A natural cut-off in the multipole space is provided by the physics of the CMB, especially by the Silk damping and the smoothing due to the thickness of the surface of last scattering. One would need sky maps with a resolution of at least this physical cut-off in order to capture all genuine CMB structures. This is currently beyond the possibilities, and one is forced to consider sky maps which are limited by the measurements, i. e. by the beam profile of the detector. The comparison of the measured sky map with a simulated map requires that the simulation is accordingly smoothed. A symmetric Gaussian smoothing kernel is sufficient for most applications which is a special case of a general symmetric smoothing kernel represented by the window function F_l. The smoothing operation is done in multipole space by

$$\delta T(\theta, \phi) \;\to\; \delta T_{F_l}(\theta, \phi) \;=\; \sum_{l=0}^{\infty} \sum_{m=-l}^{l} F_l \, a_{lm} \, Y_{lm}(\theta, \phi) \quad . \tag{6}$$

The symmetric Gaussian kernel is given by the window function

$$F_l^{\mathrm{Gauss}} \;=\; \exp\left[-\frac{\sigma_{\mathrm{g}}^2 \, l(l+1)}{2} \right] \quad , \tag{7}$$

where $\sigma_{\rm g}$ is the width of the symmetric Gaussian kernel which is usually parameterised by its full width at half maximum $\sigma_{\rm fwhm}$. The conversion formula is given by

$$\sigma_{\rm g} \;=\; \frac{\pi}{180^\circ}\,\frac{\sigma_{\rm fwhm}}{2\sqrt{2\ln(2)}} \quad , \tag{8}$$

where $\sigma_{\rm fwhm}$ is given in degrees.

An analysis of the temperature fluctuation field in position space requires a pixelization of the data on the sphere. The CMB sky maps are usually discretized in the HEALPix[18] format where every pixel covers an equal area. The resolution parameter $N_{\rm side}$ defines the total number of pixels by $N_{\rm pix}^{\rm tot} = 12\,N_{\rm side}^2$. The resolution in position space can be defined by the square root of the area of a single pixel. The area of a pixel is $10800/(\pi\,N_{\rm side}^2)$ deg^2.

The WMAP data are available in $N_{\rm side} = 512$ at the LAMBDA website (lambda.gsfc.nasa.gov), and the Planck data will be provided in $N_{\rm side} = 2048$. As a rule of thumb the pixel resolution should relate to the resolution in multipole space by $l_{\rm max} = 2N_{\rm side}$.

2.3. *Contamination of CMB measurements*

A measurement gives the genuine CMB signal superimposed with the emission of foreground sources and the detector noise.

Noise is unavoidable in measurements of CMB sky maps and acts mostly on the smallest scales, i. e. at large multipoles l. It can be modulated by generating in each pixel random fluctuations which are added to the simulated CMB signal. In the case of the WMAP data the standard deviation of the random fluctuations is proportional to $1/\sqrt{N_{\rm obs}}$ where the constant of proportionality is stated on the LAMBDA website and $N_{\rm obs}$ is the number of observations of a given pixel[19]. Since $N_{\rm obs}$ depends on the pixel, the noise also depends on the direction yielding anisotropic noise properties.

Astrophysical radiation sources bring foreground contaminations on measured CMB sky maps. Cleaning operations reduce their contributions, but cannot avoid that still some sky regions have to be excluded from the analysis by masking them out. This is a serious problem for estimators which are based on full sky information as the angular power spectrum δT_l^2. For the structure analysis the remaining foreground contamination in regions, that are not masked out, is more important since it changes the properties of the niveau lines.

3. Measures of Elongation

Probably the most common measure of the elongation of a structure is the ellipticity E which is based on the assumption that contour lines are approximated by ellipses. E is determined by the semi-axes a and b, which are real numbers with $a \geq b$, of the best-fit ellipsis. To parameterise the elongation, various dimensionless combinations

of the semi-axes can be used. Three quantities are found in the literature and given by the ellipticity E, the eccentricity ε, and a further elongation measure e. Their definitions and conversion formulas are given by

$$E := \frac{a}{b} = \sqrt{\frac{1+2e}{1-2e}} = \frac{1}{\sqrt{1-\varepsilon^2}} \quad , \quad 1 \leq E < \infty \quad , \tag{9}$$

$$\varepsilon := \frac{\sqrt{a^2-b^2}}{a} = \sqrt{1-\frac{1}{E^2}} = 2\sqrt{\frac{e}{1+2e}} \quad , \quad 0 \leq \varepsilon < 1 \quad , \text{ and} \tag{10}$$

$$e := \frac{1}{2}\frac{1-\frac{b^2}{a^2}}{1+\frac{b^2}{a^2}} = \frac{1}{2}\frac{\varepsilon^2}{2-\varepsilon^2} = \frac{1}{2}\frac{1-\frac{1}{E^2}}{1+\frac{1}{E^2}} \quad , \quad 0 \leq e < \frac{1}{2} \quad . \tag{11}$$

Larger values indicate a larger degree of elongation for all three measures. There are, however, further possibilities to quantify structures, see Section 5 and the Appendix.

4. Cosmological Dependence of Gaussian Random CMB Maps

4.1. *Number of maxima and minima*

Before we turn to the elongation at maxima and minima, we will discuss the number $N_{\max}$ and $N_{\min}$ of maxima and minima per solid angle on a 2-sphere. Assuming that the temperature fluctuations $\delta T(\hat{n})$ are given by a homogeneous and isotropic Gaussian random field, the corresponding derivations of the analytical formulae for the ensemble average of the number of maxima and minima per solid angle on a 2-sphere are given to some extent in Ref. 1, and further relations can be found in Appendix A.1.

In the case of a homogeneous and isotropic universe the distribution of $N_{\max}$ as a function of the temperature threshold δT is determined completely by the three parameters σ_0^2, σ_1^2 and σ_2^2, which are given by

$$\sigma_n^2 = \sum_l \frac{2l+1}{4\pi} C_l \left|F_l\right|^2 \frac{(l+n)!}{(l-n)!} \quad \text{with} \quad n = 0,1,2 \quad , \tag{12}$$

as discussed in the Appendix (see (A.2), (A.5) and (A.6)). Obviously these parameters can be calculated from the power spectrum of the CMB. In this subsection we consider the number $N_{\max}$ of maxima per solid angle depending on the normalised temperature $\nu := \frac{\delta T}{\sigma_0}$ where σ_0 is the standard deviation of the temperature fluctuations. The corresponding number of minima is given by the relation $N_{\min}(\nu) = N_{\max}(-\nu)$.

For a homogeneous and isotropic Gaussian random field, the distribution $N_{\max}(\nu)$ is given by

$$N_{\max}(\nu) = \frac{1}{(2\pi)^{\frac{3}{2}}\,\theta^{*2}} \exp\left[-\frac{\nu^2}{2}\right] G(\nu,\gamma,\alpha) \tag{13}$$

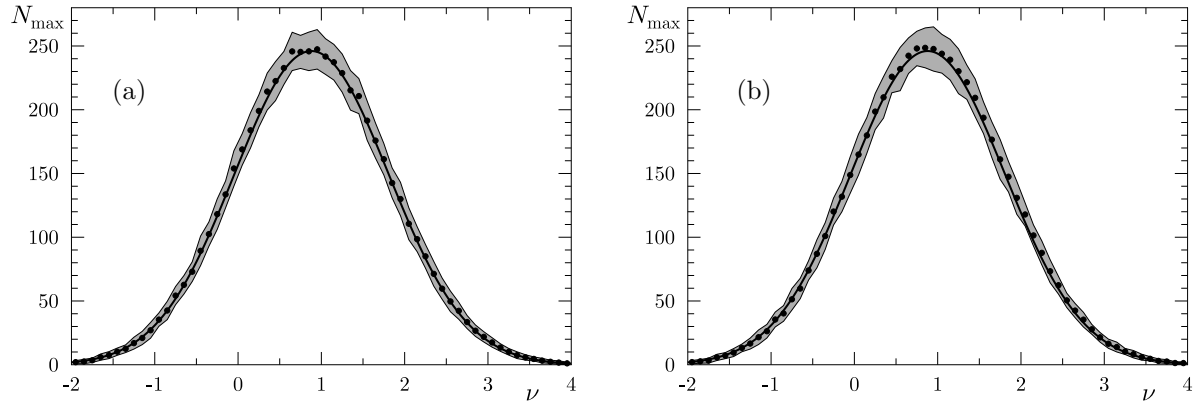

Fig. 1. The ensemble average of $N_{\max}(\nu)$ for the ΛCDM concordance model computed by Eq. (13) is shown as a solid line. Panel (a) compares this curve with the average of $N_{\max}(\nu)$ computed from 50 realisations of the infinite volume model (circles). Panel (b) shows the result obtained from 50 realisations of the torus universe with the side length $L = 3.86\, L_H$ (circles). To reveal the cosmic variance, the 1σ standard deviation is displayed as a grey band which is calculated from the corresponding 50 maps.

with

$$G(\nu,\gamma,\alpha) := \gamma\nu(1-\gamma^2)\frac{\exp\left[-\frac{\gamma^2\,\nu^2}{2(1-\gamma^2)}\right]}{\sqrt{2\,\pi\,(1-\gamma^2)}} + \left(\alpha^2(1-\gamma^2)-1+\gamma^2\nu^2\right)\left[1-\frac{1}{2}\mathrm{erfc}\left(\frac{\gamma\nu}{\sqrt{2(1-\gamma^2)}}\right)\right] + \frac{\exp\left[\frac{-\alpha^2\,\gamma^2\,\nu^2}{1+2\alpha^2(1-\gamma^2)}\right]}{\sqrt{2\alpha^2(1-\gamma^2)+1}}\left[1-\frac{1}{2}\mathrm{erfc}\left(\frac{\gamma\nu}{\sqrt{2(1-\gamma^2)(1+2\alpha^2(1-\gamma^2))}}\right)\right] \quad ,$$

and is derived in Appendix A.1, see Eq. (A.23). Here $\mathrm{erfc}(x)$ is the complementary error function. The parameters are

$$\alpha := \sqrt{1+\frac{2\sigma_1^2}{\sigma_2^2}} \quad , \quad \theta^{*2} := \alpha^2 - 1 = \frac{2\sigma_1^2}{\sigma_2^2} \quad , \quad \text{and} \quad \gamma := \frac{\sigma_1^2}{\sigma_2\,\sigma_0\,\alpha} \quad . \tag{14}$$

In Fig. 1 the theoretical distribution (13) is shown and compared with the mean value obtained from 50 CMB maps simulated at the HEALPix resolution $N_{\mathrm{side}} = 512$ using a smoothing of 1° and $l \leq 1000$. Both panels are based on the cosmological parameters of the infinite volume best-fit ΛCDM model of the WMAP data. In panel (a) the infinite model, which is isotropic, is shown, whereas panel (b) shows a multi-connected model which is anisotropic and thus does not fulfil the assumptions on which (13) is based. However, as revealed by Fig. 1(b) the data points match the distribution (13) with the same quality as in Fig. 1(a). In addition, the 50 realisations can be used to get an estimate of the cosmic variance. The corresponding

1σ standard deviation is displayed as a grey band in Fig. 1. The results for the mean value and the variance of $N_{\max}(\nu)$ for the torus universe are almost the same as for the infinite one. One could have expected this result since the number of maxima is primarily determined by the smallest scales, and a multi-connected model, which possesses in the shown case a cubic topology with a side length $L = 3.86\, L_H$, differs from the infinite one only on very large scales. Similar results are also expected in the case of other topologies, homogeneous and inhomogeneous manifolds, if the topological scales of the universe are of comparable order. Only if the volume of the universe is much smaller than the volume inside the surface of last scattering, one can expect any differences in the $N_{\max}$ distribution to those calculated in Appendix A.1. In such a case one would get an influence of the topology on small scales. But until now no hint is found in the data for a model with such a sufficiently small volume.

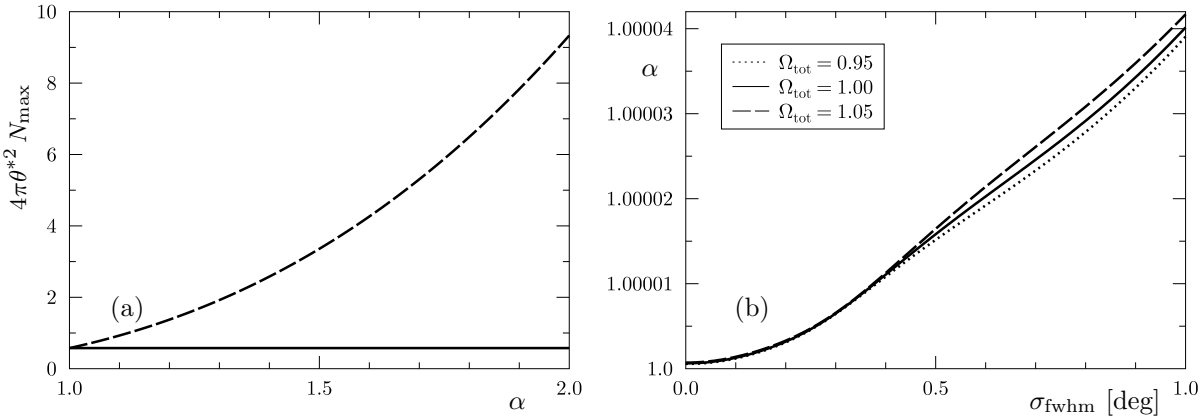

Fig. 2. In panel (a) the formula of the total number $N_{\max}$ of maxima per solid angle resulting from Equation (A1.7) in Ref. 1 (solid line) is compared to our Eq. (15) (dashed line). In panel (b) the parameter α is plotted as a function of the smoothing scale $\sigma_{\rm fwhm}$ for three cosmological models. All values of α are very close to one.

Our formulae for the various $N_{\max}$ distributions in Appendix A.1 differ by terms depending on the parameter α from the corresponding equations in Ref. 1. Here these differences are discussed using the example of the total number of maxima per solid angle. Our formula to this quantity is given by

$$N_{\max} = N_{\max}^{\rm B\&E}\, \frac{\left[\left(\alpha^2 - 1\right)\sqrt{1 + 2\alpha^2} + 1\right]\sqrt{3}}{\sqrt{1 + 2\alpha^2}} \tag{15}$$

which is derived in Appendix A.1, see (A.19). The corresponding result obtained from Equation (A1.7) in Ref. 1 is $N_{\max}^{\rm B\&E} = \frac{1}{4\pi\theta^{*2}\sqrt{3}}$, which is the leading term of the Laurent series of our Eq. (15) at $\alpha^2 = 1$. Both formulae are compared in Fig. 2(a) where $4\pi\theta^{*2}\, N_{\max}$ is displayed. In the case of $N_{\max}^{\rm B\&E}$ an α-independent, i. e. model

independent value of $\frac{1}{\sqrt{3}}$ is obtained. In contrast our result for $4\pi\theta^{*2}\,N_{\max}$ depends on α and therefore on the cosmological model since α, σ_1^2 and σ_2^2 depend on the angular power spectrum. In Fig. 2(a) we have varied $\alpha \in [1,2]$ in order to demonstrate the difference between $N_{\max}$ and the leading term $N_{\max}^{\mathrm{B\&E}}$. Is this interval of α realistic for cosmological models compatible with the measured data? To answer this question we have calculated σ_1^2 and σ_2^2 with a cut-off at $l = 1000$ with the angular power spectrum of the best-fit ΛCDM model of the WMAP data. In addition, these parameters are computed from the angular power spectrum of two models with positive and negative curvature, where the cosmological constant is varied and the other cosmological parameters are held fixed. These three cosmological models lead to different values of α, whose dependence on the smoothing scale is displayed in Fig. 2(b). One observes that α is almost equal to 1, and thus θ^{*2} is very small for all realistic cosmological parameters and smoothing scales. Therefore, we conclude that for all practical purposes the additional dependence of $4\pi\theta^{*2}\,N_{\max}$ on α is without relevance and the formulae of the $N_{\max}$ distributions in Ref. 1 are adequate.

4.2. *Elongation at Maxima and Minima*

Now we turn to the elongation measure e at maxima and minima. The ensemble average and the corresponding second moment of this quantity are given by

$$\langle e\rangle \;=\; \frac{2\alpha^2+3-\frac{3}{2}\sqrt{\frac{1+2\alpha^2}{2\alpha^2}}\ln\left[\frac{1+\sqrt{\frac{2\alpha^2}{1+2\alpha^2}}}{1-\sqrt{\frac{2\alpha^2}{1+2\alpha^2}}}\right]}{4\left[(\alpha^2-1)\sqrt{1+2\alpha^2}+1\right]} \tag{16}$$

and

$$\langle e^2\rangle \;=\; \frac{1-3\sqrt{1+2\alpha^2}+4(\sqrt{1+2\alpha^2}-1)\left(\frac{1+2\alpha^2}{2\alpha^2}\right)}{4\left[(\alpha^2-1)\sqrt{1+2\alpha^2}+1\right]}\;, \tag{17}$$

which both depend on the parameter α. The formulae are derived in the Appendix A.2. The mean value of the elongation e together with the standard deviation due to the cosmic variance is displayed in panel (a) of Fig. 3. The distribution

$$P(e) \;=\; \frac{24\,e(1-4e^2)\alpha^4\sqrt{1+2\alpha^2}}{(1+8\alpha^2e^2)^{\frac{5}{2}}\left[(\alpha^2-1)\sqrt{1+2\alpha^2}+1\right]} \tag{18}$$

of the elongation is plotted for four values of α in Fig. 3(b). This demonstrates that $P(e)$ depends on the parameter α and thus in turn via the angular power spectrum on the cosmological parameters. In this way the elongation measure e encodes some properties of the Universe.

This dependence of the elongation e on cosmological parameters is not discussed in Ref. 1. In currently admissible cosmological models the dependence on α in (A.30) can be neglected since the corresponding values of α are very close to one. The ensemble average of the elongation e is approximatively given by 0.197 for

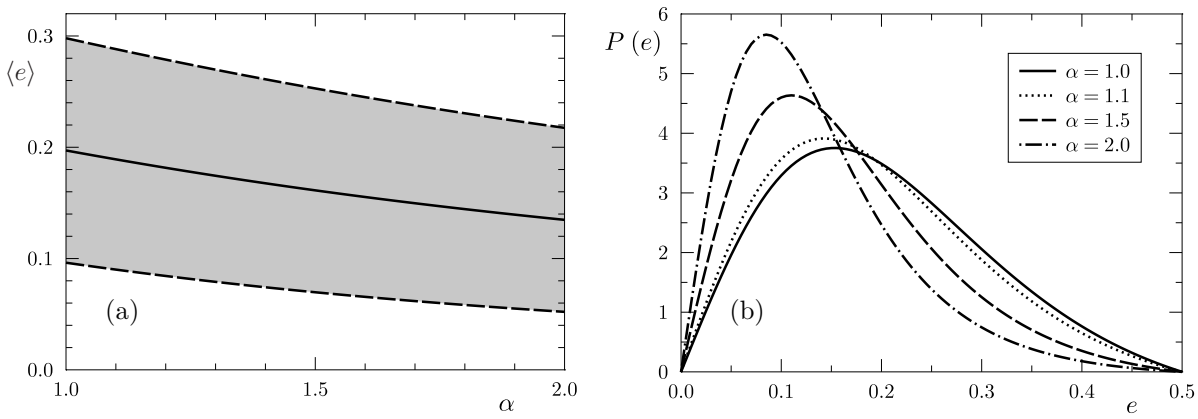

Fig. 3. In panel (a) the ensemble average of the elongation e with the corresponding 1σ standard deviation is displayed depending on the parameter α. In panel (b) the distribution $P(e)$ of the elongation e is plotted depending on the parameter α.

$\alpha = 1$. Similar results are obtained for the other elongation measures, i. e. for the ellipticity E and the eccentricity ε. The ensemble averages of these quantities are given by (A.36) and (A.33). Their values are approximately $E \approx 1.648$ and $\varepsilon \approx 0.715$ independent from the model. The cosmological influence on the elongation e, the ellipticity E or the eccentricity ε is very difficult to measure. The difficulty arises from the large cosmic variance for these quantities which is displayed as a grey band in Fig. 3(a) in the case of the elongation e. Furthermore, also the detector noise and the foregrounds in a sky map obtained by observations have an influence on the elongation, but this will be discussed later.

In addition, it is not expected that the topology of the Universe, i. e. a multi-connected spatial space, can influence the elongation of contour lines since the volumes of the fundamental cells are too large. Nevertheless, several measures of the elongation are discussed below for the special case of the cubic topology which is motivated by the fact that this model is statistically anisotropic.

5. Elongation of Hot and Cold Spots

There are different algorithms to compute the ellipticity. One method is based on the Taylor expansion of the temperature field at local maxima or minima as used in the Appendix. Alternatively, the ellipticity can be calculated by using an "inertia" tensor as described in the following.

5.1. *Computation of the ellipticity*

In the following the normalised temperature field

$$u(\hat{n}) \;=\; \frac{\delta T_{Fl}(\hat{n})}{\sigma_0} \tag{19}$$

is used. In the theoretical derivation which is outlined in the Appendix, this σ_0 is obtained by the ensemble average by using $\sigma_0 = \sqrt{C(0)}$ where $C(0)$ is the 2-point correlation function of the CMB at a separation angle $\vartheta = 0$. Such an ensemble average is not possible for a CMB sky map obtained by observations, of course, since there is only a single CMB sky from our point of view. Therefore, a sky map analysis computes the value of σ_0 from a given single sky realisation as the usual standard deviation of the temperature field

$$\sigma_0 = \sqrt{N_{\delta\Omega}^{-1} \int_{\delta\Omega} (\delta T_{F_l}(\hat{n}) - \bar{T})^2 d\Omega} \quad , \tag{20}$$

where $\bar{T}$ is the mean temperature. In the analysis of masked maps the observed area is $\delta\Omega$ and $N_{\delta\Omega}$ is the fraction of the sky that is not masked.

To get a binary image we define the excursion set of hot spots (HS) by

$$Q_\nu^{\mathrm{HS}} \;=\; \left\{\hat{n} \in \mathbb{S}^2 | u(\hat{n}) \geq \nu\right\} \quad . \tag{21}$$

Here one excludes all regions with a temperature value lower than the value of the threshold ν. Analogously the excursion set of cold spots (CS) is defined by

$$Q_\nu^{\mathrm{CS}} \;=\; \left\{\hat{n} \in \mathbb{S}^2 | u(\hat{n}) \leq \nu\right\} \quad . \tag{22}$$

The multi-connected set Q_ν can be interpreted as the union

$$Q_\nu \;=\; \bigcup_{i=1}^{N_\nu} Q_\nu^i \tag{23}$$

of the N_ν simply connected spots Q_ν^i. We compute the ellipticity for every spot Q_ν^i by using the inertia tensor defined by

$$I(Q_\nu^i) \;:=\; \begin{pmatrix} I_{xx} & I_{xy} \\ I_{yx} & I_{yy} \end{pmatrix} \;=\; \begin{pmatrix} \int\int y^2 dxdy & -\int\int yx\, dxdy \\ -\int\int xy\, dxdy & \int\int x^2 dxdy \end{pmatrix} \quad . \tag{24}$$

The spots are projected onto the xy-plane where the origin of the coordinate system matches the centre of mass of the spot Q_ν^i. The symmetric tensor $I(Q_\nu^i)$ has two real eigenvalues λ_1 and λ_2 whose relation to the ellipticity E is given by

$$E(Q_\nu^i) \;=\; \sqrt{\frac{\lambda_1}{\lambda_2}} \quad . \tag{25}$$

For the special case of an ellipse with axes a and b the eigenvalues can be computed to be

$$\lambda_1 \;=\; \frac{\pi}{4}\, a^3\, b \quad \text{and} \quad \lambda_2 \;=\; \frac{\pi}{4}\, a\, b^3 \quad \text{with} \quad \lambda_1 \geq \lambda_2 \quad . \tag{26}$$

Inserting this into (25) leads back to the definition (1), respectively (9) of the ellipticity

$$E \;=\; \frac{a}{b} \;=\; \sqrt{\frac{\lambda_1}{\lambda_2}} \quad . \tag{27}$$

The other quantities for elongation given in (10) and (11) can be obtained from the conversion formulae. The true niveau lines are not perfect ellipses, of course, but the above prescription can be used in order to obtain the ellipticity of that ellipse which approximates best the niveau line. Since there are niveau lines which deviate strongly from an ellipse one needs a further criterion to eliminate such curves in order to avoid non-sense results.

5.2. *The dependence of the ellipticity on the resolution*

The ellipticity depends sensitively on the accuracy of the sky map and care has to be taken with respect to the resolution of the map, the beam profile and the noise properties. In so far, it is not a very robust measure to characterise the CMB sky, and the details of the computation of the ellipticity have to be defined clearly in order to obtain reproducible values.

Let us at first address the issue of the resolution of the sky map. The CMB sky maps are usually stored in the HEALPix[18] format whose resolution is determined by the parameter $N_{\rm side}$. In order to determine the dependence of the ellipticity E on the value of $N_{\rm side}$, a sky map is simulated for the cubic topology using the cosmological parameters of the ΛCDM concordance model. We start with a highest resolution of $N_{\rm side} = 4096$. The sky maps are normalised such that the temperature fluctuations possess a standard deviation of 66μK, which is the value obtained from the five-year ILC map outside the KQ75 mask.

For such a simulation the ellipticity E is computed for the contour lines of a given temperature threshold δT, and the mean value is shown in Fig. 4. Contour lines that are too small are excluded since they are determined by very few pixels such that the ellipticity E is ill defined. In Fig. 4(a) the criterion is that the contour lines should at least circumference 10 pixels with respect to the chosen resolution $N_{\rm side}$. This implies that ever more small contour lines are taken into account as the value of $N_{\rm side}$ increases. Thus the mean values are computed from different sets of contour lines. This contrasts to the criterion of a fixed minimal area which leads to the result displayed in Fig. 4(b). There, all contour lines are taken into account which are larger than 10 pixels with respect to the $N_{\rm side} = 256$ resolution, i. e. all contours encompassing an area larger than $0.525\,\mathrm{deg}^2$. Thus the curve belonging to $N_{\rm side} = 256$ is the same in both panels. Whereas the exclusion criterion of a fixed pixel number leads to a robust estimation of E only at very large values of $N_{\rm side}$, the exclusion criterion of a fixed area gives consistent values already for values of $N_{\rm side}$ as small as 512. But recall from Section 4.2 that the expected ellipticity is $E \simeq 1.648$ for a Gaussian field. This value is, however, obtained with the first selection criterion which takes an increasing number of contour lines into account. This analysis thus favours the first selection criterion and, furthermore, demonstrates the sensitivity of the elongation measures.

The dependence of the ellipticity on the smoothing is not very strong. This can be inferred from Fig. 2(b) where the value of α is plotted as a function of the

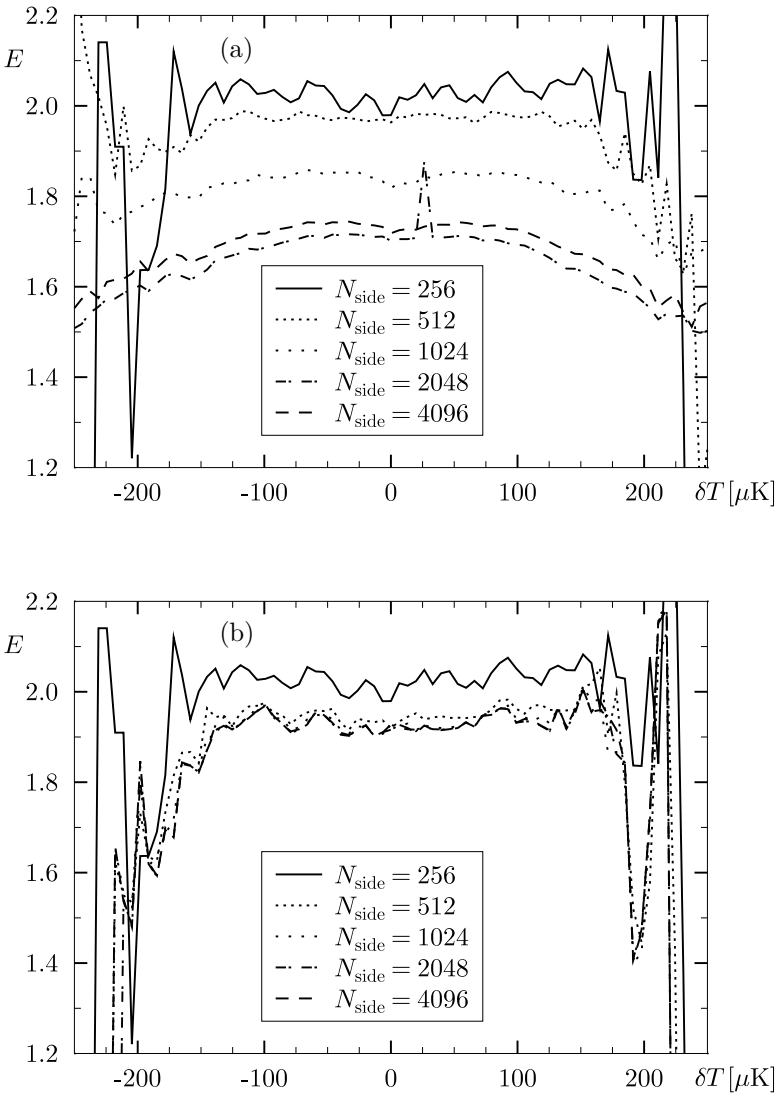

Fig. 4. The ellipticity E is computed for a realisation of the cubic universe as described in the text based on the cosmological parameters of the concordance model. The dependence on the value of $N_{\rm side}$ is presented. Panel (a) shows the ellipticity E where all contours are taken into account that enclose at least 10 pixels. The ellipticity E increases with decreasing $N_{\rm side}$. In Panel (b) all contours are selected enclosing an area of at least $0.525\,{\rm deg}^2$.

smoothing $\sigma_{\rm fwhm}$. Up to a smoothing of 1 degree all values of α are below 1.00004 and the expectation value for the ellipticity E, Eq. (A.36), is nearly constant for these smoothings. This behaviour is confirmed in Fig. 5 where different smoothings are applied to the sky maps with a fixed HEALPix resolution of $N_{\rm side} = 4096$.

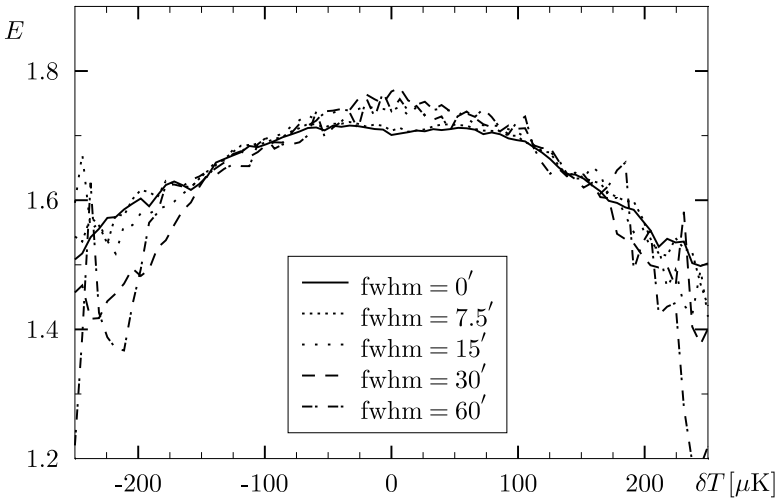

Fig. 5. For the CMB simulation used in Fig. 4(a) having the HEALPix resolution of $N_{\rm side} = 4096$, the ellipticity E is shown in dependence on the width of the Gaussian beam.

5.3. *The dependence of the elongation on the curvature*

Let us now turn to the dependence of the elongation on the curvature which is claimed[7,8,9,10,11,12] to be sufficiently strong in order to reveal the curvature of the Universe. However, in Ref. 4 no such ellipticity-curvature correlation is found. Since the elongations depend on the parameter α and thus on the cosmological parameters, such a correlation could exist. The discussion in the previous section has shown that the elongation depends on the size of the niveau lines which have to enclose at least $n_{\rm min}$ pixels. For the computation of the elongation our algorithm requires at least an area greater than 4 pixels. The number of niveau lines which can be used in a statistic depends on the normalised temperature ν. It is maximal at $\nu = \pm 1$ where the number N_ν of spots has its maximum. The values of $n_{\rm min}$ and of the normalised temperature ν are required to specify the mean ellipticity $\bar{E}(\nu, n_{\rm min})$.

The ensemble average of the elongation and the corresponding cosmic variance are computed from an ensemble of 1000 sky realisations. We analyse the excursion sets Q_ν for hot spots with thresholds $\nu > 0$ and for cold spots with thresholds $\nu < 0$. We get for every threshold ν an amount of N_ν spots with individual areas $n(Q_\nu^i)$ and elongations $e(Q_\nu^i)$. The mean ellipticity $\bar{E}(\nu, n_{\rm min})$ is computed at $\nu = 1$ by averaging the values of all spots with $n > n_{\rm min}$. This method is used in Refs. 9, 10, 11, 12. An alternative averaging is used for the mean elongation $\bar{e}(\nu, n, \Delta n)$ which is computed as a moving average around a spot size n, i. e. from spots having pixel numbers within the interval $[n - \Delta n, n + \Delta n]$. Our examination shows that these mean values are very stable with respect to the choice of the threshold ν in a range of $\nu \in [-2, 2]$.

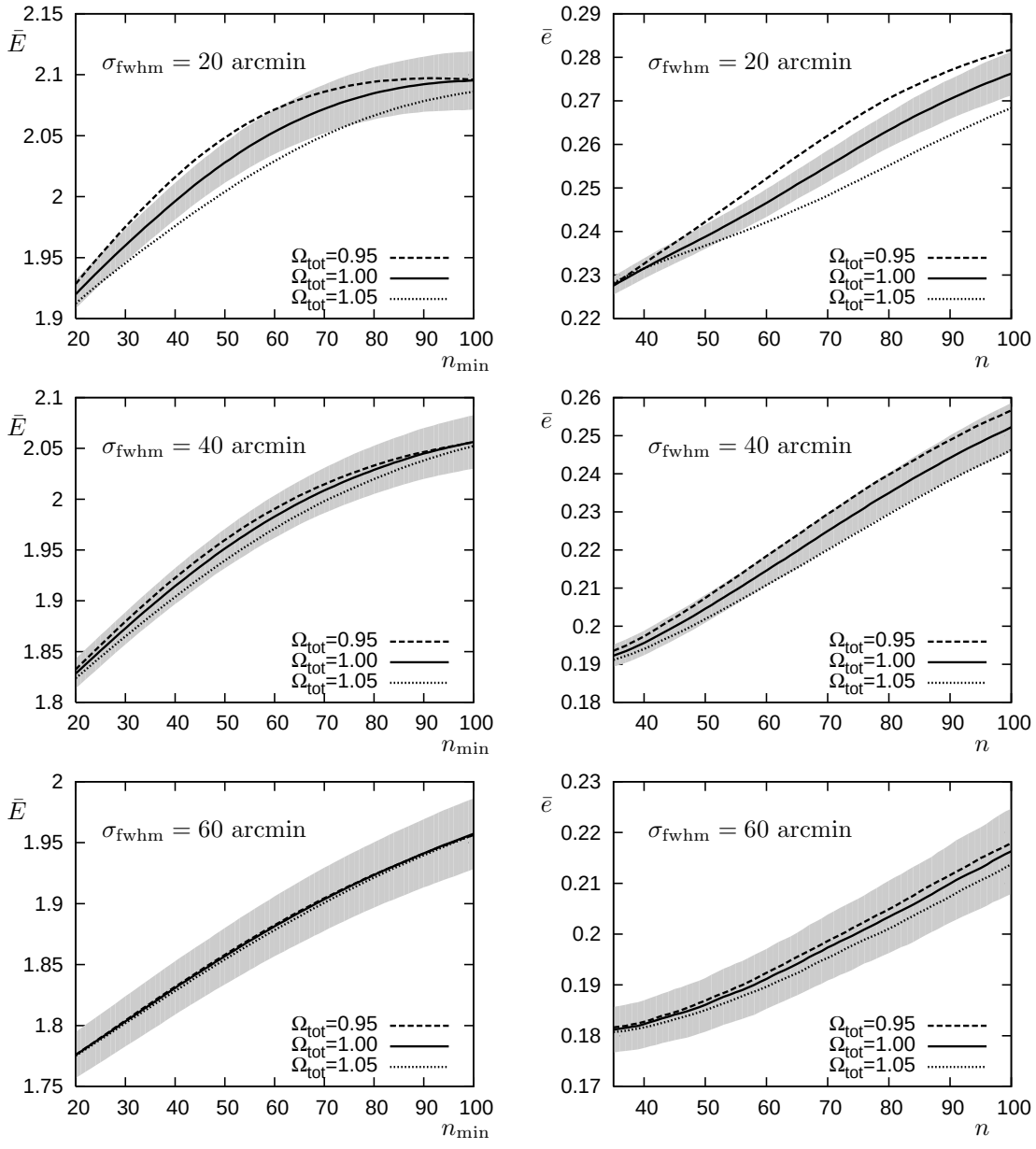

Fig. 6. The ensemble average of the mean ellipticity $\bar{E}(\nu, n_{\rm min})$ with $\nu = 1$ (left) and the mean elongation $\bar{e}(\nu, n, \Delta n)$ with $\nu = 1$ and $\Delta n = 20$ pixels (right) is computed using three Gaussian smoothing kernels (from top to bottom: $\sigma_{\rm fwhm} = 20$ arcmin, 40 arcmin, and 60 arcmin). The grey bands reflect the cosmic variance of the flat ΛCDM concordance model. The ensemble average is computed from 1000 realisations. The sky maps have a resolution of $N_{\rm side} = 512$.

In Fig. 6 the ensemble average of the mean ellipticity $\bar{E}(\nu, n_{\min})$ with $\nu = 1$ (left) and the mean elongation $\bar{e}(\nu, n, \Delta n)$ with $\nu = 1$ and $\Delta n = 20$ pixels (right) is shown. The average is computed from 1000 realisations. The sky maps possess a resolution of $N_{\text{side}} = 512$ and $l_{\max} = 1000$. The grey band reflects the cosmic variance of the flat ΛCDM concordance model (solid line). This provides the criterion whether two cosmological models can be distinguished by an elongation measure. In order to distinguish them the corresponding curves should deviate more than the width of the band due to the cosmic variance. Note that in contrast to the previous figures, the Fig. 6 displays the elongation as a function of the spot size and not of the temperature to which the niveau lines belong. This kind of plotting reveals the remarkable fact that larger spots possess a higher degree of elongation than smaller ones. This dependence is not covered by our analytical formulae which are based on the infinitesimal neighbourhood at maxima or minima. The impact of three Gaussian smoothing kernels is also investigated in Fig. 6 (from top to bottom: $\sigma_{\text{fwhm}} = 20, 40, 60$ arcmin). An increased smoothing reduces the degree of elongation. This is due to the symmetric smoothing kernel which rounds off the structures. Here the resolution of $N_{\text{side}} = 512$ does not resolve all physical structures of the Gaussian temperature field. This contrasts to Fig. 5 which is based on a sky map with a resolution of $N_{\text{side}} = 4096$ being sufficiently fine grained to resolve all structures such that the analytical formulae are applicable.

In Fig. 6 the ensemble average of the elongations is plotted for three cosmological models which differ with respect to their curvature. In addition to the flat ΛCDM concordance model, the ensemble average of a positively curved universe (dotted line) and a negatively curved universe (dashed line) is displayed. The figure reveals that a universe with negative curvature possesses a larger degree of elongation for a given spot size than the flat universe. This trend is continued for a universe with positive curvature which possesses a smaller degree of elongation for a given spot size than the flat universe. This encouraging behaviour could be used to distinguish different cosmological models if their corresponding curves differ by more than the scattering due to the cosmic variance. It turns out that this depends on the resolution of the sky maps. By applying wider smoothing kernels (from top to bottom in Fig. 6) the differences between the curves decrease and are getting insignificant compared to the cosmic variance for smoothings around $\sigma_{\text{fwhm}} = 60$ arcmin. Note that the mean elongation $\bar{e}(\nu, n, \Delta n)$ based on a moving average does a better job than the mean ellipticity $\bar{E}(\nu, n_{\min})$. This is caused by the fact that the differences in the elongation vanish for spots with a large area, and thereby their inclusion blurs the signal. The figure reveals that a resolution of at least $\sigma_{\text{fwhm}} = 20$ arcmin is necessary in order to distinguish between cosmological models having a difference in curvature of $\Delta\Omega_{\text{tot}} = 0.05$. This excludes the application of the ILC sky map of the WMAP team which has a resolution of about $\sigma_{\text{fwhm}} = 60$ arcmin. Better resolved sky maps such as the W-band maps of the WMAP team are available but they are contaminated with noise. Hence we now focus on the influence of noise on

the elongation measures.

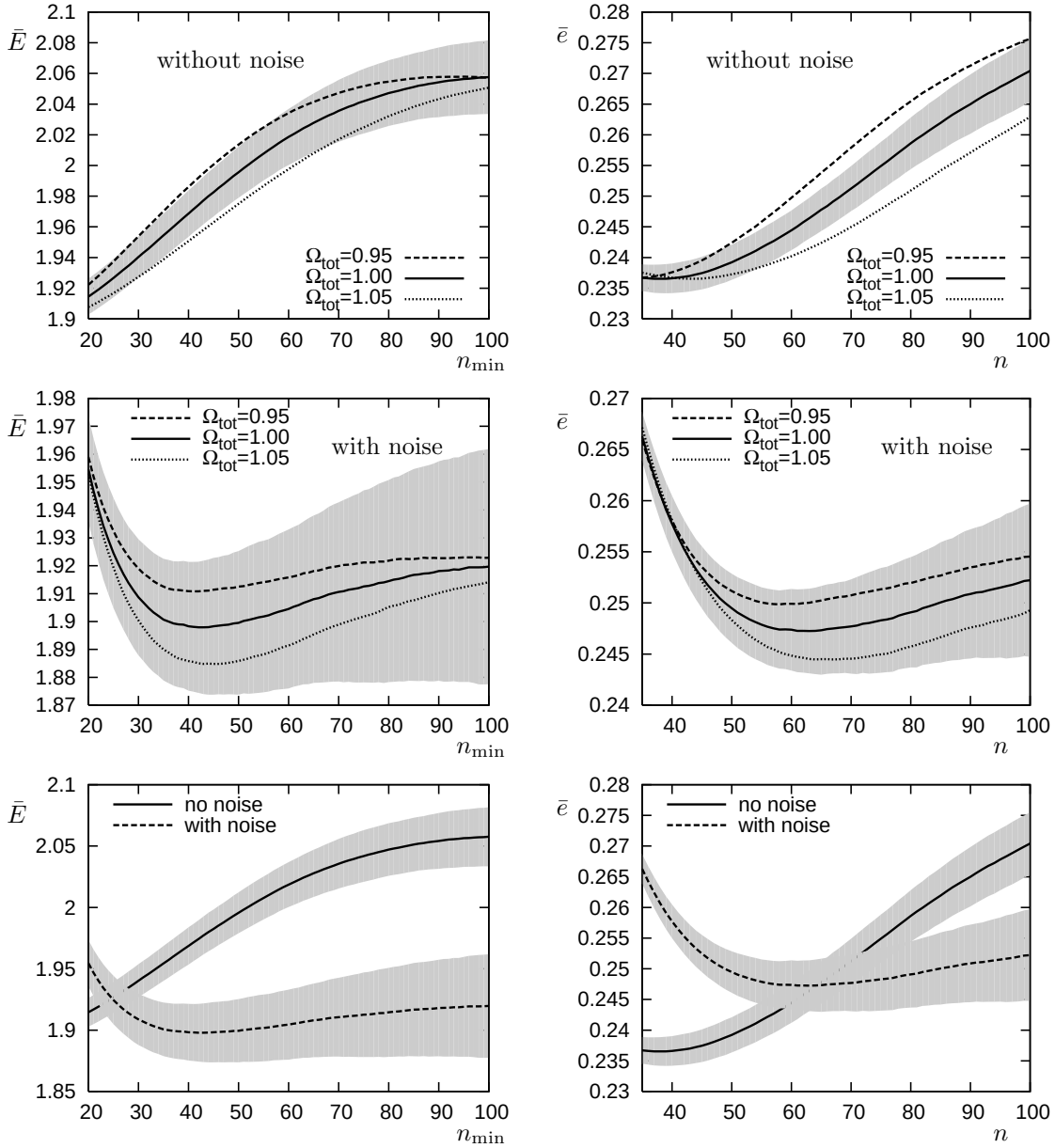

Fig. 7. The ensemble average of the mean ellipticity $\bar{E}(\nu, n_{\rm min})$ with $\nu = 1$ (left) and of the mean elongation $\bar{e}(\nu, n, \Delta n)$ with $\nu = 1$ and $\Delta n = 20$ pixels (right) is presented. These curves are obtained from 1000 sky simulations which take the window function of the W-band (channel 4) of WMAP into account. The grey bands reflect the cosmic variance of the flat ΛCDM concordance model (solid curve). The three rows give the results without noise (top), with noise (middle) and a comparison of both cases for the flat ΛCDM concordance model (bottom). The sky maps have a resolution of $N_{\rm side} = 512$.

In order to address the question whether the W-band maps are suitable for an elongation analysis, 1000 sky maps are simulated which take into account the explicit window function of the W-band (channel 4) of WMAP[20]. In Fig. 7 the ensemble averages obtained from such sky maps are shown for the mean ellipticity $\bar{E}(\nu, n_{\min})$ with $\nu = 1$ (left) and for the mean elongation $\bar{e}(\nu, n, \Delta n)$ with $\nu = 1$ and $\Delta n = 20$ pixels (right). Again the grey band reflects the cosmic variance of the flat ΛCDM concordance model (solid line). In addition, a positively curved universe (dotted line) and a negatively curved universe (dashed line) is displayed.

The upper row of Fig. 7 neglects noise completely and only takes the W-band window function into account. Both figures are similar to the two upper figures in Fig. 6 which have a resolution of $\sigma_{\mathrm{fwhm}} = 20$ arcmin comparable to that of the W-band. The mean elongation $\bar{e}(\nu, n, \Delta n)$ of spots with a small area reveals a saturation which is absent in Fig. 6. Furthermore, both elongation measures yield smaller values for spots with a larger area. This is caused by the application of the W-band window function which deviates strongly from a Gaussian. In the middle row of Fig. 7 the noise is taken into account which changes the behaviour drastically. No useful discrimination between the different curved models is possible any more. The lowest row in Fig. 7 shows a comparison for the ΛCDM concordance model with and without noise in one figure in order to emphasise the deteriorating effect of noise. A further analysis shows that an incomplete sky coverage additionally broadens the cosmic variance. Therefore, no comparison to measured data can be shown here.

Finally, we compare the infinite volume ΛCDM model with a statistically anisotropic multi-connected model for which we again choose the cubic topology with side length $L = 3.86\, L_H$. As already discussed in Section 4.1 the volume of the fundamental cell is a significant fraction of the volume inside the surface of last scattering. Therefore, only the largest angular scales are modified but not the fine structures which determine the elongation. In Fig. 8 the mean ellipticity $\bar{E}$ and the elongation $\bar{e}$ computed from 50 torus realisations are compared with the elongations of the infinite flat ΛCDM model. As expected the mean values are almost identical and their small differences are confined within the corresponding bands of cosmic variance. Thus, the anisotropy of the torus model is too weak to allow a discrimination between the models using the elongation measures.

In addition to the above investigations we also analysed our simulated sky maps at other thresholds ν. Quantitatively our statements are equivalent for hot spots and cold spots which is due to the isotropy properties of the random field. So we restrict ourselves in this paper to hot spots only. Nevertheless, if a single realisation of a measured sky map is studied, both should be combined into one statistic for a better significance. Other thresholds ν with $\nu \neq \pm 1$ possess a smaller number of spots and, therefore, lead to larger variances which is counterproductive in order to distinguish between cosmological models. Besides the mean values $\bar{E}(\nu, n_{\min})$ and $\bar{e}(\nu, n, \Delta n)$ we also studied higher moments, higher central moments and their statistical interpretations. Since it turns out that the mean value provides the most

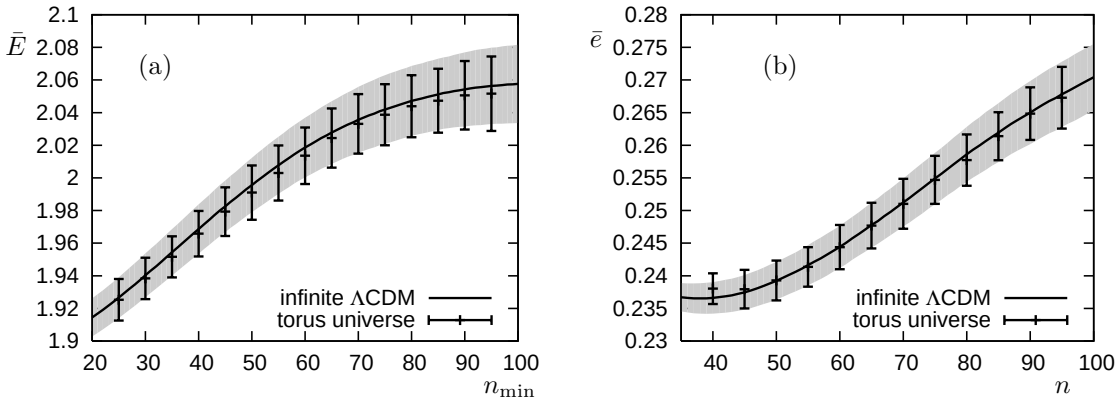

Fig. 8. The ensemble average of the mean ellipticity $\bar{E}(\nu, n_{\min})$ with $\nu = 1$ (left) and of the mean elongation $\bar{e}(\nu, n, \Delta n)$ with $\nu = 1$ and $\Delta n = 20$ pixels (right) is presented. The elongations E and e of the infinite ΛCDM model are shown as a solid curve and its cosmic variance as a grey band calculated from 1000 realisations. The elongations of the torus universe with $L = 3.86\, L_H$ are shown as error bars which represent the cosmic variance based on 50 sky simulations. In both cases the window function of the W-band (channel 4) of WMAP is taken into account, but the noise is neglected. The sky maps have a resolution of $N_{\text{side}} = 512$.

robust measure we restrict our discussion to them here. The moving average applied in $\bar{e}(\nu, n, \Delta n)$ leads to the best discrimination between cosmological models, but the additional parameter Δn has to be chosen adequately, since too small values result in small spot numbers (lack on statistics) and too large values result in a blurring caused by large spots.

6. Summary

In this paper the structures of CMB sky maps are studied with respect to the crucial question whether these structures betray some information about the underlying cosmological model. There are various quantities to analyse the structures of the niveau lines and the focus is put on the elongation which can be described by the ellipticity E, Eq. (9), or the elongation measure e defined in Eq. (11). The elongation depends on the parameter α, Eq. (14), which in turn depends on the multipole spectrum C_l and thus on the cosmology. The theoretical dependence of various elongation measures on α is given for the case that the statistical properties of the temperature field are those of two-dimensional homogeneous and isotropic Gaussian random fields. Our analysis leads to the conclusion that this dependence, however, is weak. Since the resolution of the maps has a superior influence on the niveau lines, the results obtained from sky maps depend on the pixelization and on the beam profile of the detector. Both deteriorating restrictions are analysed. It is found that the elongation cannot be analysed without reference to the pixelization and the beam profile.

The dependence of the elongation on the cosmological parameters can be in-

vestigated for niveau lines classified either by their temperature or by the area which they encompass. The curvature of the universe is revealed by the elongation as demonstrated in Fig. 6, where the elongation is considered as a function of the size of the spots. The best discrimination between cosmological models is obtained by applying the moving average to $\bar{e}(\nu, n, \Delta n)$. A resolution of at least $\sigma_{\mathrm{fwhm}} = 20$ arcmin is required in order to distinguish between cosmological models which differ in the curvature by $\Delta\Omega_{\mathrm{tot}} = 0.05$. This excludes the analysis of the ILC map of the WMAP team, whose resolution is three times lower. The required resolution is achieved by the W-band sky map which has, however, much stronger noise. The analysis of simulated maps with the noise properties of the W-band map shows that it is also not suitable for this investigation. The Planck mission will provide maps with a significantly higher resolution as well as lower noise such that there is the hope that the results of that mission can be analysed with respect to the structure properties of the CMB.

We also study the elongation properties of a multi-connected space form, i. e. a model of the universe having a non-trivial topology, because it is not statistically isotropic and thus violates the assumptions which have to be satisfied for the analytical expressions to be valid. No distinction is found between the trivial topology, i. e. the concordance model, and the non-trivial topology with respect to the elongation. This is expected since the topology modifies the physics on the largest scales and has thus only a modest influence on the elongation. At least as long as the fundamental cell is so large that it constitutes a significant fraction within the surface of last scattering. Thus the best prospects for elongation measures can be found in the detection of curvature.

Appendix A. The Gaussian Random Field and the CMB

In this Appendix, we outline the derivation of the peak density and the ellipticity of the temperature fluctuations $\delta T(\hat{n})$ of the CMB under the assumption that the temperature fluctuations behave as a homogeneous and isotropic Gaussian random field

$$f(\delta T(\hat{n})) = \frac{1}{\sqrt{2\pi\sigma_0^2}} \exp\left(-\frac{|\delta T(\hat{n})|^2}{2\sigma_0^2}\right) \tag{A.1}$$

on the 2-dimensional sphere. Here $\sigma_0^2(\hat{n}) := \langle \delta T(\hat{n})\, \delta T(\hat{n}) \rangle$ is the variance of the temperature fluctuations. In an isotropic model σ_0^2 is independent of the direction $\hat{n}$ and is given in that case by

$$\sigma_0^2 = \sum_l \frac{(2l+1)}{4\pi} C_l |F_l|^2 = C(0) \quad . \tag{A.2}$$

The ensemble average is specified as $\langle ... \rangle$, F_l accounts for the appearance of a beam profile and $C(0)$ is the correlation function of the temperature fluctuations in a homogeneous and isotropic universe at a separation angle $\vartheta = 0$. To use a compact

notation in this Appendix, the subscript F_l at the temperature field δT_{F_l} is omitted. This index stands for the smoothing operation (6). The following derivations and notations are based on Ref. 1.

The temperature fluctuation $\delta T(\hat{n})$ close to the direction $\hat{n}'$ on the 2-sphere is given by the Taylor series

$$\delta T(\hat{n}) = \delta T(\hat{n}') + [\nabla_i \delta T(\hat{n})]_{\hat{n}=\hat{n}'}(x^i - x'^i) + \frac{[\nabla_i \nabla_j \delta T(\hat{n})]_{\hat{n}=\hat{n}'}}{2}(x^i - x'^i)(x^j - x'^j) + \ldots \quad . \tag{A.3}$$

∇_i is the covariant derivative on the 2-sphere with respect to the coordinate x^i. In the sequel we will choose $x^1 = \theta$ and $x^2 = \phi$. The corresponding line element is given by $ds^2 = d\theta^2 + \sin^2\theta d\phi^2$. The associated covariant metric is $\gamma_{11} = 1$, $\gamma_{22} = \sin^2\theta$ and $\gamma_{ij} = 0$ otherwise. Therefore the Christoffel symbols are $\Gamma^2_{12} = \Gamma^2_{21} = \frac{\cos\theta}{\sin\theta}$, $\Gamma^1_{22} = -\sin\theta\cos\theta$ and $\Gamma^k_{ij} = 0$ otherwise.

The Taylor series (A.3) can be written in a compact way by introducing the variables $\delta T = \delta T(\hat{n})$, $\eta_i = \eta_i(\hat{n}) := \nabla_i \delta T(\hat{n})$ and $\zeta_{ij} = \zeta_{ij}(\hat{n}) := \nabla_i \nabla_j \delta T(\hat{n})$. Calculating the symmetric correlation matrix for Gaussian random fields with respect to the ensemble average in a homogeneous and isotropic model, one obtains

$$\begin{aligned} &\langle \delta T \delta T \rangle = \sigma_0^2, \quad \langle \delta T \eta_i \rangle = 0, \quad \langle \eta_i \eta_j \rangle = \frac{\sigma_1^2}{2}\gamma_{ij}, \quad \langle \delta T \zeta_{ij} \rangle = -\frac{\sigma_1^2}{2}\gamma_{ij}, \\ &\langle \eta_i \zeta_{js} \rangle = 0, \quad \langle \zeta_{ij}\zeta_{rs} \rangle = \frac{\sigma_2^2}{8}\left[\gamma_{ij}\gamma_{rs} + \gamma_{is}\gamma_{rj} + \gamma_{js}\gamma_{ir}\right] + \frac{\sigma_1^2}{2}\gamma_{ij}\gamma_{rs} \end{aligned} \tag{A.4}$$

with

$$\sigma_1^2 := \sum_l \frac{(2l+1)}{4\pi} C_l |F_l|^2 l(l+1) \tag{A.5}$$

and

$$\sigma_2^2 := \sum_l \frac{(2l+1)}{4\pi} C_l |F_l|^2 (l-1)l(l+1)(l+2) \quad . \tag{A.6}$$

Appendix A.1. *The peak density of the CMB*

Now the formulae for the number of extrema per solid angle are derived from the density of extrema $n_{\rm ext}(\hat{n}) = \sum_p \delta(\hat{n} - \hat{n}_p)$ for an isotropic and homogeneous Gaussian random temperature field $\delta T(\hat{n})$ on the 2-sphere. The density of extrema turns out to be given by

$$n_{\rm ext}(\hat{n}) = \delta(\vec{\eta}(\hat{n}))\ |\det(\zeta(\hat{n}))| \tag{A.7}$$

by using $x^i - x^i{}_p \approx \eta_j(\hat{n})\left(\zeta^{ji}\right)^{-1}(\hat{n}_p)$. Here $\hat{n}_p$ denotes the directions of the extrema.

We choose $\theta = \frac{\pi}{2}$ without loss of generality. We transform ζ_{ij} onto its principal coordinate system by a rotation with an angle $\tilde{\theta}$, thus obtaining the diagonal form $-\mathrm{diag}(\lambda_1, \lambda_2)$, ordered by $|\lambda_1| \geq |\lambda_2|$. At maxima or minima of the temperature field the eigenvalues λ_1 and λ_2 have both positive or both negative values, respectively.

At saddle points one of these eigenvalues is positive and the other is negative. In the following only maxima and minima are considered. The eigenvalues of the Hessian contain slightly different information as the eigenvalues of the inertia tensor of the area enclosed by the contour lines which are used to calculate the ellipticity E in Section 5. Now with the eigenvalues λ_1 and λ_2, the following variables are defined

$$x := \frac{\lambda_1 + \lambda_2}{\sigma_2\,\alpha} \;, \qquad e := \frac{\lambda_1 - \lambda_2}{2\,(\lambda_1 + \lambda_2)} = \frac{\lambda_1 - \lambda_2}{2\,\sigma_2\,\alpha\,x} \;, \tag{A.8}$$

in terms of which the Hessian ζ_{ij} reads

$$\zeta_{11} = -\frac{\sigma_2\,x\,\alpha}{2}\Big[1 + 2\,e\,\cos(2\tilde{\theta})\Big] \;, \tag{A.9}$$

$$\zeta_{22} = -\frac{\sigma_2\,x\,\alpha}{2}\Big[1 - 2\,e\,\cos(2\tilde{\theta})\Big] \;, \tag{A.10}$$

$$\zeta_{12} = -\sigma_2\,x\,\alpha\,e\,\sin(2\tilde{\theta}) \;, \tag{A.11}$$

where $\alpha := \sqrt{1 + \frac{2\,\sigma_1^2}{\sigma_2^2}}$ and e is the elongation, Eq. (11). It should be noted that in Ref. 1 e is termed ellipticity. In general these new variables are restricted to $\tilde{\theta} \in [0, \pi]$, $x \in (-\infty, \infty)$ and $e \in [0, \infty)$. In case of extrema the interval of the elongation is confined to $e \in [0, \frac{1}{2})$.

The transformation of the volume element in ζ-space is

$$d\zeta_{11} d\zeta_{22} d\zeta_{12} \;=\; 2\,\sigma_2^3\,\alpha^3\,x^2\,dx\,de\,d\tilde{\theta} \;. \tag{A.12}$$

The probability distribution for the variables $\nu := \frac{\delta T}{\sigma_0}$, $\vec{\eta}$, x, e, and $\tilde{\theta}$ is given by

$$\begin{aligned} P(\nu, \vec{\eta}, x, e, \tilde{\theta})\,de\,dw\,dx\,d\tilde{\theta}\,d^2\vec{\eta} = \exp\left[-\frac{w^2}{2}\right] \exp\left[-\left(\frac{1}{2} + 4e^2\alpha^2\right) x^2\right] \\ \times\; \exp\left[-\frac{\vec{\eta}^{\,2}}{\sigma_1^2}\right]\; 8\;(\alpha x)^2\;e\,de\,\frac{dw}{\sqrt{2\,\pi}}\,\frac{dx}{\sqrt{2\,\pi}}\,\frac{d\tilde{\theta}}{\pi}\,\frac{d^2\vec{\eta}}{\pi\sigma_1^2} \end{aligned} \tag{A.13}$$

where the result is simplified by using the variable $w := \frac{\nu - \gamma x}{\sqrt{1-\gamma^2}}$ and introducing the abbreviation $\gamma := \frac{\sigma_1^2}{\sigma_2\,\sigma_0\,\alpha}$. γ is determined by the power spectrum. Here w and x are independent and normalised $\langle x^2\rangle = 1$, $\langle w^2\rangle = 1$.

As a result of the restriction to positive eigenvalues $\lambda_1 \geq \lambda_2 \geq 0$, i.e. restricting to maxima, one obtains $x \in [0, \infty)$ and $e \in [0, \frac{1}{2})$. Using this, $\theta^{*2} := \frac{2\,\sigma_1^2}{\sigma_2^2} = \alpha^2 - 1$ and

$$\det(\zeta) = \frac{1}{4}\,\sigma_2^2\,x^2\,\alpha^2\,(1 - 4\,e^2) \quad , \tag{A.14}$$

we obtain for the mean differential density of maxima

$$\begin{aligned} N_{\max}(\nu,x,e,\tilde{\theta}) \;=\; & \int_{-\infty}^{\infty} dw' \int_{\mathbb{R}^2} d^2\vec{\eta}\,' \int_0^{\infty} dx' \int_0^{\frac{1}{2}} de' \int_0^{\pi} d\tilde{\theta}\,'\; P(\nu',\vec{\eta}\,',x',e',\tilde{\theta}') \\ & \times\delta(\vec{\eta}\,')\,\delta(x'-x)\,\delta(e'-e)\,\delta(\tilde{\theta}\,'-\tilde{\theta})\,\frac{1}{4}\,\sigma_2^2\,x'^2\,\alpha^2\,(1-4\,e'^2) \\ = & \frac{2}{\pi^3\,\theta^{*2}\,\sqrt{1-\gamma^2}} e\,\left(1-4e^2\right)(\alpha x)^4 \exp\left[-\frac{w^2}{2}\right] \\ & \times \exp\left[-\left(\frac{1}{2}+4e^2\alpha^2\right)x^2\right] \quad . \end{aligned} \tag{A.15}$$

The integration over the orientation angle $\tilde{\theta}$ yields ($w = w(x,\nu)$)

$$\begin{aligned} N_{\max}(\nu,x,e) = & \frac{2}{\pi^2\,\theta^{*2}\,\sqrt{1-\gamma^2}} e\,\left(1-4e^2\right)(\alpha x)^4 \exp\left[-\frac{w^2}{2}\right] \\ & \times\; \exp\left[-\left(\frac{1}{2}+4e^2\alpha^2\right)x^2\right] \quad . \end{aligned} \tag{A.16}$$

An integration over ν in the last expression results in

$$N_{\max}(x,e) = \frac{1}{\theta^{*2}}\left(\frac{2}{\pi}\right)^{\frac{3}{2}} (\alpha x)^4\, e\left(1-4e^2\right)\exp\left[-\left(\frac{1}{2}+4e^2\alpha^2\right)x^2\right] \tag{A.17}$$

where we have substituted the variable ν by w. A further integration over x yields

$$N_{\max}(e) = \frac{6\,e\left(1-4e^2\right)\alpha^4}{\theta^{*2}\pi\left(1+8\alpha^2e^2\right)^{\frac{5}{2}}} \quad . \tag{A.18}$$

Here we have used the substitution $y = \left(\frac{1}{2}+4e^2\alpha^2\right)x^2$. A final integration over e leads to the total number of maxima per solid angle

$$\begin{aligned} N_{\max} = \int_0^{\frac{1}{2}} de\, N_{\max}(e) \;=\; & \frac{3a^4}{8\pi\theta^{*2}}\;{}_2F_1(1,\frac{5}{2};3;-2\alpha^2) \\ = & \frac{\left(\alpha^2-1\right)\sqrt{1+2\alpha^2}+1}{4\pi\theta^{*2}\sqrt{1+2\alpha^2}} \\ = & N_{\max}^{\mathrm{B\&E}}\,\frac{\left[\left(\alpha^2-1\right)\sqrt{1+2\alpha^2}+1\right]\sqrt{3}}{\sqrt{1+2\alpha^2}} \end{aligned} \tag{A.19}$$

where $N_{\max}^{\mathrm{B\&E}} := \frac{1}{4\pi\theta^{*2}\sqrt{3}}$ is the limiting case derived in Ref. 1. We achieved the first representation of $N_{\max}$ by using the substitution $y = e^2$ and the integral (2.2.6.15) in Ref. 21 for the hypergeometric function ${}_2F_1(a,b;c;z)$.

Integrating Eq. (A.16) with respect to x and using Eq. (2.3.15.3) in Ref. 21 or

Eq. (2.3.15.7) in Ref. 21, we obtain two representations of $N_{\max}(\nu, e)$,

$$\begin{aligned} N_{\max}(\nu,e) &= \frac{48\left(1-\gamma^2\right)^2\,\alpha^4\,e\left(1-4e^2\right)}{\pi^2\,\theta^{*2}\left(8e^2\alpha^2\left(1-\gamma^2\right)+1\right)^{\frac{5}{2}}} \\ &\qquad \times \exp\left[-\nu^2\,\frac{2\left(8e^2\alpha^2\left(1-\gamma^2\right)+1\right)-\gamma^2}{4\left(1-\gamma^2\right)\left(8e^2\alpha^2\left(1-\gamma^2\right)+1\right)}\right] \\ &\qquad \times D_{-5}\left(\frac{-\gamma\nu}{\sqrt{\left(1-\gamma^2\right)\left(8e^2\alpha^2\left(1-\gamma^2\right)+1\right)}}\right) \\ &= \frac{\sqrt{2\pi}e\left(1-4e^2\right)\alpha^4}{\pi^2\,\theta^{*2}\sqrt{8e^2\alpha^2\left(1-\gamma^2\right)+1}}\exp\left[-\frac{\nu^2}{2\left(1-\gamma^2\right)}\right] \\ &\qquad \times \frac{\partial^4}{\partial q^4}\left[\exp\left[\frac{q^2}{4p}\right]\operatorname{erfc}\left(\frac{q}{2\sqrt{p}}\right)\right] \end{aligned} \tag{A.20}$$

with $q = -\frac{\gamma\nu}{\sqrt{1-\gamma^2}}$ and $p = \frac{8e^2\alpha^2\left(1-\gamma^2\right)+1}{2(1-\gamma^2)}$. $D_\alpha(x)$ is the parabolic cylinder function and $\operatorname{erfc}(x)$ the complementary error function.

Integrating Eq. (A.16) over e, one gets

$$N_{\max}(\nu,x) = \frac{1}{4\pi^2\,\theta^{*2}\sqrt{1-\gamma^2}}\exp\left[-\frac{w^2}{2}\right]\exp\left[-\frac{x^2}{2}\right]f(x) \tag{A.21}$$

with $f(x) := \exp\left[-\left(\alpha x\right)^2\right] - 1 + \left(\alpha x\right)^2$. An integration of Eq. (A.21) over ν or x yields

$$N_{\max}(x) = \frac{1}{(2\pi)^{\frac{3}{2}}\,\theta^{*2}}\exp\left[-\frac{x^2}{2}\right]f(x) \tag{A.22}$$

and

$$N_{\max}(\nu) = \frac{1}{(2\pi)^{\frac{3}{2}}\,\theta^{*2}}\exp\left[-\frac{\nu^2}{2}\right]\,G(\nu,\gamma,\alpha) \tag{A.23}$$

with

$$\begin{aligned} G(\nu,\gamma,\alpha) := {} & \gamma\nu(1-\gamma^2)\frac{\exp\left[-\frac{\gamma^2\,\nu^2}{2(1-\gamma^2)}\right]}{\sqrt{2\,\pi\,(1-\gamma^2)}} \\ & + \left(\alpha^2(1-\gamma^2)-1+\gamma^2\nu^2\right)\left[1-\frac{1}{2}\operatorname{erfc}\left(\frac{\gamma\nu}{\sqrt{2(1-\gamma^2)}}\right)\right] \\ & + \frac{\exp\left[\frac{-\alpha^2\,\gamma^2\,\nu^2}{1+2\alpha^2(1-\gamma^2)}\right]}{\sqrt{2\alpha^2(1-\gamma^2)+1}}\left[1-\frac{1}{2}\operatorname{erfc}\left(\frac{\gamma\nu}{\sqrt{2(1-\gamma^2)(1+2\alpha^2(1-\gamma^2))}}\right)\right] \quad , \end{aligned}$$

respectively. We have used the integral (2.3.15.7) in Ref. 21 and the relation $\operatorname{erfc}(-x) = 2 - \operatorname{erfc}(x)$ in order to compute $N_{\max}(\nu)$.

The mean differential density of maxima depending on the eccentricity $\varepsilon := \sqrt{1-\lambda_2/\lambda_1} \equiv 2[e/(1+2e)]^{1/2}$ ($\varepsilon \in [0,1)$) is given by

$$N_{\max}(\varepsilon) \;=\; \frac{3\sqrt{2}\,\varepsilon^3(1-\varepsilon^2)}{\pi\,\theta^{*2}\,\alpha\left(\frac{(2-\varepsilon^2)^2}{2\alpha^2}+\varepsilon^4\right)^{\frac{5}{2}}} \tag{A.24}$$

and depending on the ellipticity $E := \sqrt{\lambda_1/\lambda_2} \equiv [(1+2e)/(1-2e)]^{1/2}$ ($E \in [1,\infty)$) by

$$N_{\max}(E) = \frac{24\,\alpha^4\,E^3(E^2-1)}{\pi\,\theta^{*2}[E^4(1+2\alpha^2)+2\,E^2\,(1-2\alpha^2)+(1+2\alpha^2)]^{\frac{5}{2}}} \quad . \tag{A.25}$$

We obtain the corresponding expressions for the mean differential densities of the minima from those of the maxima by replacing ν by $-\nu$ and x by $-x$, e.g. $N_{\min}(\nu) = N_{\max}(-\nu)$. Using this we get the combined distribution

$$\begin{aligned}(N_{\max}+N_{\min})\,(\nu) = {} & \frac{1}{(2\pi)^{\frac{3}{2}}\,\theta^{*2}}\exp\left[-\frac{\nu^2}{2}\right] \\ & \times\left[\left(\alpha^2(1-\gamma^2)-1+\gamma^2\nu^2\right)+\frac{\exp\left[\frac{-\alpha^2\,\gamma^2\,\nu^2}{1+2\alpha^2(1-\gamma^2)}\right]}{\sqrt{2\alpha^2(1-\gamma^2)+1}}\right] \quad .\end{aligned} \tag{A.26}$$

In addition to the formulae given in Ref. 1, we have specified here analytical expressions for the densities $N_{\max}(x,e)$, $N_{\max}(x)$, $N_{\max}(e)$, $N_{\max}(\varepsilon)$ and $N_{\max}(E)$. It should be pointed out that the formulae in Ref. 1 are obtained by the leading term of the Laurent series of our formulae at $\alpha^2 = 1$. As discussed in Section 4, the parameter α contains information about the underlying cosmology.

Appendix A.2. *The ellipticity in the CMB*

In the following the formulae for the moments of the ellipticity E, the eccentricity ε and the elongation e at local maxima of an isotropic and homogeneous Gaussian random temperature field on a 2-sphere are derived. In the case of local minima the resulting formulae are also valid. The elongation which is considered in this Appendix results from a Taylor expansion at local extrema and can be computed from the eigenvalues of the Hessian (A.8). For this reason the elongation e contains only information from local maxima or local minima. The same is valid for the ellipticity E and the eccentricity ε, because they are related to the elongation by Eqs. (9) and (10), respectively. This is a difference to the definition of the ellipticity in Section 5 where the eigenvalues of the inertia tensor of the area enclosed by the contour lines are used to calculate the ellipticity.

Using the mean differential densities of the maxima with respect to the various arguments derived in Appendix A.1, one can define the distribution of a variable u subject to the constraint parameter z,

$$P(u|z) \;=\; \frac{N_{\max}(u,z)}{N_{\max}(z)} \quad , \tag{A.27}$$

e.g. $P(e|\nu) = N_{\max}(\nu, e)/N_{\max}(\nu)$ with the variable e and the parameter ν.

The expectation values of the moments of the ellipticity with respect to the distribution

$$\begin{aligned} P(e) = \frac{N_{\max}(e)}{N_{\max}} &= \frac{24\, e(1-4e^2)\alpha^4\sqrt{1+2\alpha^2}}{(1+8\alpha^2e^2)^{\frac{5}{2}}\left[(\alpha^2-1)\sqrt{1+2\alpha^2}+1\right]} \\ &= \frac{16\, e(1-4e^2)}{(1+8\alpha^2e^2)^{\frac{5}{2}}\ {}_2F_1(1,\frac{5}{2};3;-2\alpha^2)} \end{aligned} \tag{A.28}$$

are given by

$$\langle e^n\rangle = \int_0^{\frac{1}{2}} de\, P(e)\, e^n = \frac{B(\frac{n}{2}+1,2)\ {}_2F_1(\frac{n}{2}+1,\frac{5}{2};\frac{n}{2}+3;-2\alpha^2)}{2^{n-1}\ {}_2F_1(1,\frac{5}{2};3;-2\alpha^2)}\ . \tag{A.29}$$

$B(x,y)$ is the beta function. We get $P(e)$ by using Eqs. (A.18) and (A.19) and the moments by applying the integral (2.2.6.15) in Ref. 21. From the expression of the moments, the mean value ($n = 1$) results in

$$\begin{aligned} \langle e\rangle &= \frac{2\alpha^2+3-\frac{3}{2}\sqrt{\frac{1+2\alpha^2}{2\alpha^2}}\ln\left[\frac{1+\sqrt{\frac{2\alpha^2}{1+2\alpha^2}}}{1-\sqrt{\frac{2\alpha^2}{1+2\alpha^2}}}\right]}{4\left[(\alpha^2-1)\sqrt{1+2\alpha^2}+1\right]} \\ &= 0.197 - 0.041\ (\alpha^2-1) + \ \mathrm{O}((\alpha^2-1)^2) \end{aligned} \tag{A.30}$$

and the second moment ($n = 2$) in

$$\begin{aligned} \langle e^2\rangle &= \frac{1-3\sqrt{1+2\alpha^2}+4(\sqrt{1+2\alpha^2}-1)\left(\frac{1+2\alpha^2}{2\alpha^2}\right)}{4\left[(\alpha^2-1)\sqrt{1+2\alpha^2}+1\right]} \\ &= 0.049 - 0.018\ (\alpha^2-1) + \ \mathrm{O}((\alpha^2-1)^2) \end{aligned} \tag{A.31}$$

of the ellipticity at maxima.

Using Eqs. (A.24) and (A.19) we obtain the distribution

$$\begin{aligned} P(\varepsilon) &= \frac{N_{\max}(\varepsilon)}{N_{\max}} \\ &= \frac{96\,\alpha^4\sqrt{1+2\alpha^2}\,\varepsilon^3(1-\varepsilon^2)}{\left[(\alpha^2-1)\sqrt{1+2\alpha^2}+1\right](4-4\varepsilon^2+(1+2\alpha^2)\varepsilon^4)^{\frac{5}{2}}} \end{aligned} \tag{A.32}$$

from which the mean value

$$\begin{aligned} \langle\varepsilon\rangle &= \int_0^1 d\varepsilon\, P(\varepsilon)\,\varepsilon \\ &= 0.715 - 0.059\ (\alpha^2-1) + \ \mathrm{O}((\alpha^2-1)^2) \end{aligned} \tag{A.33}$$

and the second moment

$$\begin{aligned}\langle\varepsilon^2\rangle &= \int_0^1 d\varepsilon\, P(\varepsilon)\,\varepsilon^2 \\ &= \frac{2\left(\alpha^2+1-\sqrt{1+2\alpha^2}\right)}{(\alpha^2-1)\sqrt{1+2\alpha^2}+1} \\ &= 0.536 - 0.083\ (\alpha^2-1) + \ \mathrm{O}((\alpha^2-1)^2) \end{aligned} \tag{A.34}$$

of the eccentricity can be calculated.

Using Eqs. (A.25) and (A.19) one gets the distribution

$$\begin{aligned} P(E) &= \frac{N_{\max}(E)}{N_{\max}} \\ &= \frac{96\,\alpha^4\sqrt{1+2\alpha^2}\,E^3(E^2-1)}{\left[(\alpha^2-1)\sqrt{1+2\alpha^2}+1\right]\left(1+2\alpha^2+2(1-2\alpha^2)E^2+(1+2\alpha^2)E^4\right)^{\frac{5}{2}}}\ , \end{aligned} \tag{A.35}$$

which leads to the mean value

$$\begin{aligned}\langle E\rangle &= \int_1^\infty dE\, P(E)\, E \\ &= \frac{2}{\sqrt{3}} - \sqrt{3}K(\sqrt{2}i) + \frac{2}{\sqrt{3}}E(\sqrt{2}i) \\ &\quad + \left[-2+\frac{10}{\sqrt{3}\,3}+\left(-\frac{1}{2\sqrt{3}}+3\right)K(\sqrt{2}i)+\left(\frac{5}{6\sqrt{3}}-2\right)E(\sqrt{2}i)\right](\alpha^2-1) \\ &\quad + \mathrm{O}((\alpha^2-1)^2) \\ &= 1.648 - 0.217\ (\alpha^2-1) + \ \mathrm{O}((\alpha^2-1)^2) \end{aligned} \tag{A.36}$$

and the second moment of the ellipticity E

$$\begin{aligned}\langle E^2\rangle &= \int_1^\infty dE\, P(E)\, E^2 \\ &= \frac{(1+2\alpha^2)^{\frac{3}{2}}(\alpha^2+1)+4\alpha^4-4\alpha^2-1}{\left[(\alpha^2-1)\sqrt{1+2\alpha^2}+1\right](1+2\alpha^2)} \\ &= 3.131 - 0.980\ (\alpha^2-1) + \ \mathrm{O}((\alpha^2-1)^2)\ . \end{aligned} \tag{A.37}$$

Here $K(k)$ is the complete elliptic integral of the first kind, $E(k)$ the complete elliptic integral of the second kind and k the modulus.

All these moments of the ellipticity E, the elongation e and the eccentricity ε depend on α. On the other hand α is determined by the angular power spectrum of the underlying model, see Eq. (14). For this reason also the moments of the ellipticity E, the elongation e and the eccentricity ε depend on the angular power spectrum of the model. This dependence is considered in Section 4.2.

Acknowledgements

We would like to thank the Deutsche Forschungsgemeinschaft for financial support (AU 169/1-1). H. S. J. would like to thank the graduate school "Analysis of complexity, information and evolution" of the Land Baden-Württemberg for the stipend.

CMBFAST (www.cmbfast.org), HEALPix[18] (healpix.jpl.nasa.gov) and the WMAP data from the LAMBDA website (lambda.gsfc.nasa.gov) were used in this work.

References

1. J. R. Bond and G. Efstathiou, Mon. Not. R. Astron. Soc. **226**, 655 (1987).
2. O. Doré, S. Colombi, and F. R. Bouchet, Mon. Not. R. Astron. Soc. **344**, 905 (2003), arXiv:astro-ph/0202135.
3. C. Monteserín, R. B. Barreiro, E. Martínez-González, and J. L. Sanz, Mon. Not. R. Astron. Soc. **371**, 312 (2006), arXiv:astro-ph/0604356.
4. R. B. Barreiro, J. L. Sanz, E. Martínez-Gonzále, L. Cayón, and J. Silk, Astrophys. J. **478**, 1 (1997), arXiv:astro-ph/9612114.
5. R. B. Barreiro, E. Martínez-González, and J. L. Sanz, Mon. Not. R. Astron. Soc. **322**, 411 (2001), arXiv:astro-ph/0009365.
6. C. Monteserín, R. B. Barreiro, J. L. Sanz, and E. Martínez-González, Mon. Not. R. Astron. Soc. **360**, 9 (2005), arXiv:astro-ph/0511308.
7. V. G. Gurzadyan and S. Torres, Astron. & Astrophys. **321**, 19 (1997), arXiv:astro-ph/9610152.
8. V. G. Gurzadyan *et al.*, Int. J. of Mod. Phys. D **12**, 1859 (2003), arXiv:astro-ph/0210021.
9. V. G. Gurzadyan *et al.*, Mod. Phys. Lett. **A20**, 491 (2005), arXiv:astro-ph/0312305.
10. V. G. Gurzadyan *et al.*, Nuovo Cim. **118B**, 1101 (2003), arXiv:astro-ph/0402399.
11. V. G. Gurzadyan *et al.*, Mod. Phys. Lett. **A20**, 813 (2005), arXiv:astro-ph/0503103.
12. V. G. Gurzadyan, C. L. Bianco, A. L. Kashin, H. Kuloghlian, and G. Yegorian, Phys. Lett. **A363**, 121 (2007), arXiv:astro-ph/0607160.
13. D. N. Spergel *et al.*, Astrophys. J. Supp. **170**, 377 (2007), astro-ph/0603449.
14. E. Komatsu *et al.*, Astrophys. J. Supp. **180**, 330 (2009), arXiv:astro-ph/0803.0547.
15. R. Aurich, H. S. Janzer, S. Lustig, and F. Steiner, Class. Quant. Grav. **25**, 125006 (2008), arXiv:0708.1420 [astro-ph].
16. R. Aurich, Class. Quant. Grav. **25**, 225017 (2008), arXiv:0803.2130 [astro-ph].
17. R. Aurich, S. Lustig, and F. Steiner, Class. Quant. Grav. **27**, 095009 (2010), arXiv:0903.3133 [astro-ph].
18. K. M. Górski *et al.*, Astrophys. J. **622**, 759 (2005), HEALPix web-site: http://healpix.jpl.nasa.gov/.
19. C. L. Bennett *et al.*, Astrophys. J. Supp. **148**, 1 (2003), astro-ph/0302207.
20. R. S. Hill *et al.*, Astrophys. J. Supp. **180**, 246 (2009), arXiv:arXiv:0803.0570 [astro-ph].
21. A. P. Prudnikov, Y. A. Brychkov, and O. I. Marichev, *Integrals and series, Volume 1: Elementary Functions* (Gordon and Breach Science Publishers, 1966), Translated from Russian by N. M. Queen.